Optical and orbital characterization of spherically symmetric static black holes of self-gravitating new nonlinear electrodynamics model

İlim İrfan Çimdiker,[1,2,*] Ali Övgün,[3,†] and Yosef Verbin[2,‡]

[1]Institute of Physics, University of Szczecin, Wielkopolska 15, 70-451 Szczecin, Poland
[2]Astrophysics Research Center, the Open University of Israel, Raanana 4353701, Israel
[3]Physics Department, Eastern Mediterranean University, Gazimagusa 99628 via Mersin 10, Turkiye

(Received 17 March 2026; accepted 18 June 2026; published 13 July 2026)

Horizon-scale imaging and precision lensing have turned black holes into quantitative laboratories for strong gravity and for nonstandard electromagnetic physics. We study the optical appearance and orbital dynamics of a new class of static spherically symmetric black holes sourced by a Palatini-inspired nonlinear electrodynamics model, minimally coupled to Einstein-Hilbert gravity. Using a unified geodesic analysis, we identify the key radii that organize the strong-field phenomenology. For photons we determine the unstable photon sphere, the associated critical capture threshold, and the resulting shadow size for a distant observer, and we map how these observables respond to the charge and to the nonlinearity index n. For massive probes we compute circular orbits and the innermost stable circular orbit, clarifying the departure from the Schwarzschild and Reissner-Nordström cases. We then connect to classical tests by evaluating the light deflection angle and periastron advance, providing additional diagnostics that complement the shadow. Our results furnish a practical reference model for confronting first-order nonlinear electrodynamics black holes with current and forthcoming imaging and lensing data.

DOI: 10.1103/p6lp-rktr

I. INTRODUCTION

Black holes (BHs) provide an unparalleled arena to confront general relativity (GR) with observations in the strong-field regime. The past decade has witnessed a qualitative shift from indirect evidence to horizon-scale probes: precision astrometry of stellar orbits around Sgr A* has revealed relativistic orbital precession consistent with GR expectations [1], while the Event Horizon Telescope (EHT) has delivered horizon-scale images of the shadow-casting region of M87* and Sgr A* [2,3]. Complementary frameworks have developed the use of horizon-scale imaging and strong-field electromagnetic probes to test the Kerr hypothesis and constrain non-GR deformations across a broad class of scenarios, including parametrized metrics and environment-sensitive shadow models [4–16]. These developments motivate a systematic exploration of how beyond-GR effects and nonstandard matter sectors can imprint themselves on null geodesics, photon regions, lensing observables, and shadow morphology, thereby enabling model selection (or exclusion) with increasing observational leverage. Recent work argues that "spacetime collisions" can exhibit a distinctly electrodynamic character, motivating strong-field tests that treat electromagnetic nonlinearities as dynamical players rather than small corrections [17].

From a theoretical standpoint, BH shadows encode the boundary between captured photon trajectories and those reaching a distant observer. In asymptotically flat spacetimes this boundary is closely tied to critical impact parameters and the structure of photon spheres or photon regions [18–20]. In parallel, gravitational lensing in both weak and strong deflection regimes provides complementary observables, including deflection angles, relativistic images, and time delays, whose analytic characterization has proven especially powerful for discriminating between nearby spacetimes [21–25]. The modern literature emphasizes that, beyond the idealized "shadow" of geometric optics, observable features, such as photon rings and lensing rings, depend on astrophysical emission models, nevertheless, the underlying geometric criticality remains a robust diagnostic of the metric in the near-horizon region [19,26]. A concrete example in this direction is the rotating Einstein-Euler-Heisenberg black hole, where nonlinear electrodynamics modifies both the shadow morphology and the quasinormal mode spectrum in a correlated way [27]. Related analyses of nonlinearly charged black holes connect horizon-scale imaging with accretion physics by jointly modeling the shadow and thin disk observables across the model parameter space [28].

A particularly well-motivated class of departures from the Einstein-Maxwell paradigm arises when the

*Contact author: ilim.cimdiker@phd.usz.edu.pl
†Contact author: ali.ovgun@emu.edu.tr
‡Contact author: verbin@openu.ac.il

electromagnetic sector is promoted to a nonlinear electrodynamics (NLED) theory. Historically, NLED was introduced to regularize diverging classical fields and self-energies (as in Born-Infeld electrodynamics) and it also appears as an effective description of quantum vacuum polarization in strong fields (Euler-Kockel-Heisenberg), thereby providing a controlled framework for strong-field phenomenology [29–32]. When coupled to gravity, NLED can significantly modify black hole spacetimes and their causal/optical structure [33–36], and in particular it can support regular (nonsingular) geometries, such as those suggested by Bardeen [37] and Hayward [38]. Besides the original Einstein-NLED interpretation of the Bardeen spacetime, later developments showed that broader construction schemes in Einstein-NLED accommodate whole families of regular black holes, including both the Bardeen and Hayward geometries as special cases of a common framework [39–45]. For completeness, we also note that the Fan-Wang construction was followed by critical comments and clarifications concerning the interpretation of parameters and the consistency of the associated NLED description [46,47].

Regular/NLED-supported solutions and their generalizations have also been constructed in broader settings, including higher-dimensional and Lovelock gravities and related nonlinear Maxwell sectors, enlarging the space of analytic strong-field templates beyond four-dimensional Einstein-Hilbert theory [48–51]. Beyond regularity, NLED theories exhibit additional structural features, including electric-magnetic duality rotations and $SL(2,\mathbb{R})$-type invariances in axion-dilaton extensions, which further enrich their gravitational sector [52,53]. Moreover, NLED light propagation is governed by an effective optical geometry, so that NLED light rays can deviate from metric null geodesics, inducing characteristic corrections to lensing and shadow observables [54,55]. These optical effects have direct phenomenological counterparts in lensing/shadow studies of Born-Infeld-type black holes and plasma-modified propagation, strengthening the link between NLED microphysics and observable ray-tracing signatures [56,57]. Moreover, the regularity program has been extended to rotating spacetimes and to alternative constructions where NLED fields source nonsingular rotating black holes, with corresponding implications for photon regions and shadow shapes [58–62]. These motivations become even sharper in the EHT era: horizon-scale imaging of M87* and Sgr A* provides direct constraints on non-Einsteinian/charged compact-object scenarios [2,3,63], with dedicated analyses showing that the 2017 EHT data can bound effective charges and related couplings [64,65] and that magnetically charged/NLED black holes can be confronted with EHT measurements [66]. In parallel, analytic developments have clarified the relation between the shadow edge, photon rings, and lensing rings as robust probes of near-horizon geometry [19,20,26], while recent studies emphasize that NLED effects can imprint coherently across several channels, such as shadows, deflection angles, quasinormal spectra, and graybody factors, enabling multiobservable consistency tests [67,68]. Related model-building directions include NLED coupled to modified-gravity sectors [e.g., Palatini $f(R)$ or $f(R)$-NLED realizations], as well as other regularization mechanisms, such as higher-curvature (quadratic) gravity, which collectively broaden the landscape of nonsingular compact objects worth confronting with strong-field observables [69–73].

In this context, recently a new family of nonlinear gauge-field theories has been constructed by adopting a first-order (Palatini-inspired) formulation for linear and nonlinear electrodynamics, in which the field strength and potential are treated as *a priori* independent variables [74,75]. Within this framework, Verbin *et al.* [75] obtained new self-gravitating solutions, including spherically symmetric black holes, and identified a "Palatini-inspired NLED" (PINLED) model as a minimal and analytically tractable representative exhibiting novel features in both flat space and in the self-gravitating case. Since the phenomenological discriminant power of such solutions ultimately hinges on observables, it is timely to develop a detailed optical and orbital characterization of these geometries.

The aim of this paper is to provide a systematic analysis of the gravitational optics and kinematics of the static, spherically symmetric black hole solutions of a family of PINLED models minimally coupled to Einstein-Hilbert gravity. Concretely, we (i) determine the photon sphere structure and the associated critical impact parameter controlling capture versus escape, (ii) compute the shadow radius as perceived by an observer at infinity and map its dependence on the NLED charge and the nonlinearity index n, and (iii) complement these horizon-scale diagnostics with classical tests, such as light deflection and periastron precession, enabling cross-validation against both weak-field and strong-field constraints. Our results are presented in a form suited for direct comparison with the Schwarzschild (S) and Reissner-Nordström (RN) limits, and for integration into broader frameworks that confront modified-gravity/NLED scenarios with EHT and lensing data [2,3,21,64,65].

Beyond furnishing concrete predictions for a new analytic family of NLED black holes, the broader importance of this work is methodological and phenomenological: it illustrates how first-order NLED constructions translate into sharp optical signatures, and it strengthens the bridge between model building in strong-field gravity and the rapidly maturing observational program targeting the horizon-scale structure. As data quality improves, such theoretically controlled templates will be essential for turning shadow and lensing measurements into precision tests of fundamental physics.

II. PINLED BLACK HOLES

The Palatini-inspired variant of NLED (PINLED) stands on the basic principle that a theory of vector field may be constructed in terms of a gauge potential A_μ and an antisymmetric tensor field $P_{\mu\nu}$, which are independent of each other. The theory is of first order in the sense that the Lagrangian contains only first derivatives of A_μ through the gauge invariant combination $F_{\mu\nu} \equiv \partial_\mu A_\nu - \partial_\nu A_\mu$ (or $F \equiv dA$). In order to obtain the field equations of the theory, the dynamical variables A_μ and $P_{\mu\nu}$ are varied independently of each other.

This is actually a family of Lagrangians that are determined by an arbitrary *defining function* of the first four of the six scalars, which may be constructed as bilinear products of $F_{\mu\nu}$ and $P_{\mu\nu}$ and their duals ${}^*F^{\mu\nu} = \epsilon^{\mu\nu\rho\sigma}F_{\rho\sigma}/2\sqrt{-g}$ and ${}^*P^{\mu\nu}$ (defined analogously),

$$Y = P^{\mu\nu}F_{\mu\nu}, \quad Z = P^{\mu\nu}P_{\mu\nu}, \quad \Upsilon = F_{\mu\nu}{}^*P^{\mu\nu},$$
$$\Omega = P_{\mu\nu}{}^*P^{\mu\nu}, \quad X = F^{\mu\nu}F_{\mu\nu}, \quad \Xi = F_{\mu\nu}{}^*F^{\mu\nu}. \tag{2.1}$$

We write, therefore, the Lagrangian density (J^μ is a possible current),

$$\mathcal{L}_{\mathrm{PINLED}} = \mathcal{K}(Z, \Omega, Y, \Upsilon) - J^\mu A_\mu, \tag{2.2}$$

which gives rise to the following field equations:

$$-2\nabla_\mu(\mathcal{K}_Y P^{\mu\nu} + \mathcal{K}_\Upsilon{}^*P^{\mu\nu}) = J^\nu,$$
$$2(\mathcal{K}_Z P^{\mu\nu} + \mathcal{K}_\Omega{}^*P^{\mu\nu}) + \mathcal{K}_Y F^{\mu\nu} + \mathcal{K}_\Upsilon{}^*F^{\mu\nu} = 0. \tag{2.3}$$

The defining function is of course not entirely arbitrary, but must obey some physical constraints. The conventional practice in the first-order formulation of NLED is to impose the condition that the first-order theory with the defining function $\mathcal{K}(Z, \Omega, Y, \Upsilon)$ is equivalent to a certain second-order NLED theory [75,76]. However, the new PINLED family is a wider family of NLED Lagrangians free of this limiting constraint [74,75].

Although we give up this limiting constraint, there are still physical constraints to be fulfilled, but we will not pause here for a full study of this issue. We will specify only one example, which is the existence of the Maxwell limit. This will be evidently the case in the simple PINLED Lagrangian, which we choose to study here from now on. In this Lagrangian the nonlinearity originates from the Y^n term of the otherwise linear defining function $\mathcal{K}(Z, \Omega, Y, \Upsilon) = Z/4 - Y/2 + \gamma Y^n/(2n)$. More explicitly, we write the Lagrangian of the "PINLED Y^n model" (or "Y^n model" for short) as

$$\mathcal{L}^{(1)}_{Y^n} = \frac{1}{4}P^{\mu\nu}P_{\mu\nu} - \frac{1}{2}P^{\mu\nu}F_{\mu\nu} + \frac{\gamma}{2n}(P^{\mu\nu}F_{\mu\nu})^n - J^\mu A_\mu, \tag{2.4}$$

where γ is a real parameter. It is clear that for $\gamma = 0$, this reduces to the first-order version of Maxwell's theory and $P_{\mu\nu} = F_{\mu\nu}$.

Now, variations with respect to A_μ and $P_{\mu\nu}$ give the modified source-full "Maxwell" equations and the $P - F$ relations,

$$\nabla_\mu(W(Y)P^{\mu\nu}) = J^\nu, \qquad P_{\mu\nu} = W(Y)F_{\mu\nu},$$
$$\text{where } W(Y) \equiv 1 - \gamma Y^{n-1}. \tag{2.5}$$

Adding the Einstein-Hilbert term $R/2\kappa$ to the Y^n Lagrangian yields a dynamical gravitational field, which is determined by the Einstein equations

$$G_{\mu\nu} = -\kappa T_{\mu\nu},$$
$$T_{\mu\nu} = -W^2 F_{\mu\alpha}F_\nu{}^\alpha - \frac{g_{\mu\nu}}{2}\left[\frac{n-2}{2n}W - \frac{n-1}{n}\right]Y. \tag{2.6}$$

Next we assume spherically symmetric electrostatic solutions of the field Eqs. (2.5)–(2.6). This means that the only nonvanishing field components are $F_{tr}(r) = -F_{rt}(r)$ and $P_{tr}(r) = -P_{rt}(r)$ and the metric tensor can be written in the form $g_{\mu\nu} = \mathrm{diag}(f(r), -1/f(r), -r^2, -r^2\sin^2\theta)$. The NLED field equations can be solved analytically for F_{tr} and P_{tr} in parametric form with the variable Y in the role of the parameter [75],

$$\begin{cases} F_{tr} = \sqrt{-Y/2W(Y)} \\ r = \left(\frac{2Q^2}{-YW^3(Y)}\right)^{1/4} \end{cases}, \qquad \begin{cases} P_{tr} = \sqrt{-W(Y)Y/2} \\ r = \left(\frac{2Q^2}{-YW^3(Y)}\right)^{1/4} \end{cases}. \tag{2.7}$$

Notice that for electric fields, $Y \leq 0$. The energy-momentum components of this electrostatic solution can be obtained from the expression for T^ν_μ in (2.6) as

$$T^r_r = T^0_0 = -\frac{1}{4}Y + \frac{3n-2}{4n}\gamma Y^n,$$
$$T^\theta_\theta = T^\varphi_\varphi = \frac{1}{4}Y + \frac{n-2}{4n}\gamma Y^n, \tag{2.8}$$

and their r dependence can be obtained exactly as in Eq. (2.7). We observe that the energy density is positive definite as long as $(-1)^n\gamma > 0$, which is the assumption we will take from now on.

This solution in (2.7) has the same form in flat spacetime as well. For further details we refer the reader to Ref. [75] and note here only that the electric field does not diverge as $r \to 0$. For $n = 2$, $F_{tr}(0)$ is finite, while for all $n \geq 3$ it is zero. The total field energy is always finite.

For the next stages of the discussion it will be much more convenient to transform to dimensionless quantities: the electric components will be rescaled with a parameter $\mathfrak{E}$, which has units of electric field, defined by $|\gamma| = 1/\mathfrak{E}^{2(n-1)}$, and the quantities with dimensions of length like r, M, and Q will be rescaled by the length parameter $\ell = 1/\sqrt{\kappa\mathfrak{E}^2}$, such that $\varrho = r/\ell$, $m = M/\ell$, and $q = \kappa\mathfrak{E}Q$. Within this dimensionless framework we will write the dimensionless,

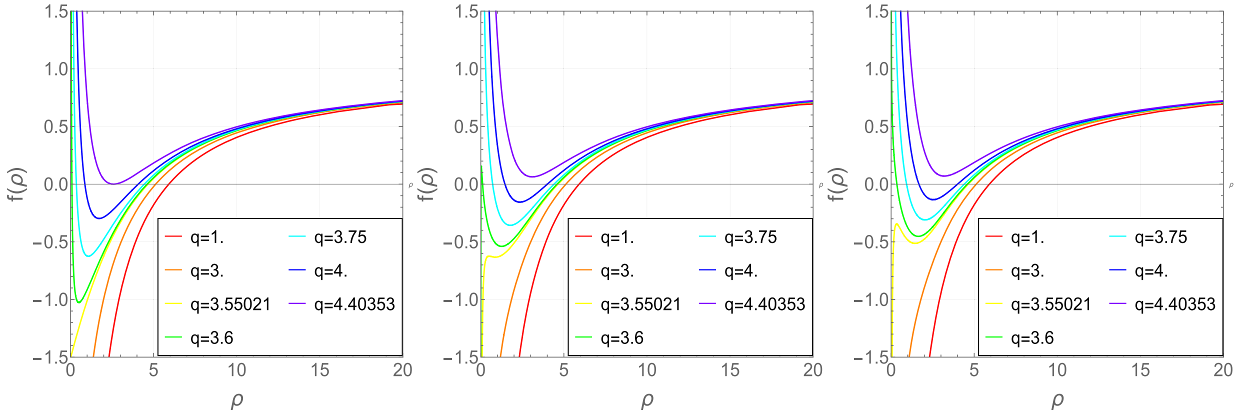

(a) $n=2$ (b) $n=3$ (c) $n=4$

FIG. 1. Lapse function $f(\rho)$ of BH solutions of the PINLED Y^n model with various values of q for n values $n=2,3,4$ with $m_{\rm BH}=3$. Notice the curves of maximal charge, which correspond to an extremal BH for $n=2$, but naked singularity solutions for larger n.

static, spherically symmetric metric in terms of the single free (lapse) function $f(\rho)$ as

$$ds^2 = f(\rho)dt^2 - \frac{1}{f(\rho)}d\rho^2 - \rho^2(d\theta^2 + \sin^2\theta\, d\phi^2). \tag{2.9}$$

For such a metric, Einstein's equations reduce to a single first-order equation,

$$\frac{1}{\rho^2}\frac{d}{d\rho}[\rho(1-f)] = K(\rho) \Rightarrow \frac{dm}{d\rho} = \frac{\rho^2}{2}K(\rho), \tag{2.10}$$

where the dimensionless mass function $m(\rho)$ is defined by $f(\rho) = 1\text{–}2m(\rho)/\rho$, and $K(\rho)$ is the energy density in dimensionless form. For the PINLED Y^n black holes discussed here, the solution for the lapse function is written in a parametric representation with $y = -Y/\mathfrak{E}^2$ as a parameter,

$$\begin{cases} f(y) = 1 - \frac{2m(y)}{\rho(y)}, \\ \rho(y) = \left(\frac{2q^2}{y(1+y^{n-1})^3}\right)^{1/4}, \end{cases} \tag{2.11}$$

after we also transformed the second equation of (2.10) to an equation for $m(y)$ using the explicit expression for the dimensionless energy density $K(y)$,

$$K(y) = \frac{y}{4} + \frac{3n-2}{4n}y^n. \tag{2.12}$$

The solution for the mass function is given by

$$m(y) = \frac{q^{3/2}}{2^{1/4}\cdot 15(n-1)}\left[\frac{n(17n-49) + (10+n(27n-101))y^{n-1} - 32ny^{2(n-1)}}{4n(1+y^{n-1})^{9/4}}y^{1/4} + \frac{8}{y^{(n-2)/4}}F\left(\frac{1}{4}, \frac{n-2}{4(n-1)}, \frac{5n-6}{4(n-1)}, -\frac{1}{y^{n-1}}\right)\right] + m_{\rm BH} - \bar{m}_{\rm field}, \tag{2.13}$$

where $F(a,b,c,z)$ is the hypergeometric function, $m_{\rm BH}$ is the black hole mass, and $\bar{m}_{\rm field}$ is the (finite) total accumulated field mass in all space. This field mass is expressed as

$$\bar{m}_{\rm field} = \frac{2^{3/4}q^{3/2}}{3}\cdot\frac{\Gamma(\frac{4n-3}{4(n-1)})\Gamma(\frac{5n-6}{4(n-1)})}{\Gamma(\frac{9}{4})}. \tag{2.14}$$

In Figs. 1 and 2, one can see the profiles of the lapse function and the horizon ρ_H as a function of $m_{\rm BH}$ with different values of q and n. PINLED Y^n black holes exhibit Schwarzschild-like solutions (with one horizon) for small charges, and Reissner-Nordström-like (RN-like) solutions (with two horizons) for larger charges. In Fig. 2 we limit the n values to $n=2,3$ since the differences for higher n's are difficult to notice in this resolution. For similar reasons related to graphical resolution, we will avoid analogous graphic presentation of $n\geq 4$ results in the rest of the paper, but we will still present them in tables and describe their features in the text. The lower branches of the RN-like curves of Fig. 2 correspond to the inner horizons. The more relevant to this paper is the event horizon, which is the exterior if the number of horizons is larger than 1. Thus, we will usually refer to the event horizon simply as "horizon" and take some care when distinction is needed. These two branches are separated by a

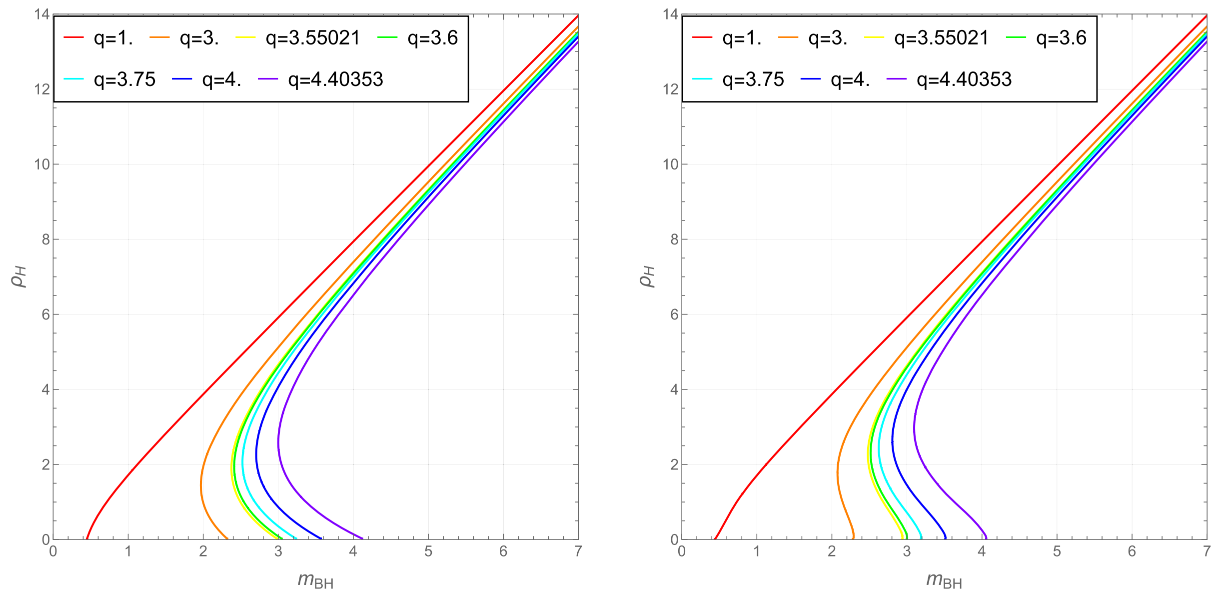

(a) $n = 2$ (b) $n = 3$

FIG. 2. Horizon radius ρ_H versus black hole mass m_{BH} for Y^n BHs with various values of q for $n = 2$ and 3. Notice that $q = 4.40353$ is the EBH charge for $m_{\mathrm{BH}} = 3$ and $n = 2$, but corresponds to naked singularity solutions for $n = 3$.

point where the inner and external horizons merge. This defines an extremal black hole (EBH), which corresponds to the minimal mass for a given charge, or complementarily, to the maximal charge for a given mass. For larger n, the EBH charge decreases. As expected, for fixed BH mass the charge q always reduces the horizon radius, while for fixed charge the mass increases the horizon radius.

III. TIMELIKE AND NULL GEODESICS AROUND Y^n BLACK HOLES

For the study of timelike and null geodesics around the Y^n BHs we will follow the standard procedure by first writing the geodesic equation and identifying the constants of motion in the equatorial plane $\theta = \pi/2$. To this end, we define the Lagrangian as $\mathcal{L}_p = \Lambda/2$, where

$$\Lambda = -g_{\mu\nu}\dot{x}^\mu \dot{x}^\nu = -f(\rho)\dot{t}^2 + \frac{\dot{\rho}^2}{f(\rho)} + \rho^2\dot{\phi}^2, \tag{3.1}$$

where the dot represents the derivative with respect to an affine parameter. This Lagrangian immediately yields two conserved quantities: the energy $E = f(\rho)\dot{t}$ and the angular momentum $L = \rho^2\dot{\phi}$. The Lagrangian itself is also constant along geodesics, $\Lambda = -\xi$. By an affine transformation, we can choose $\xi = \{1, 0\}$ for massive and massless particles, respectively. This allows us to write the radial equation in the form of a one-dimensional mechanical energy equation for a point particle,

$$\dot{\rho}^2 + V_{\mathrm{eff}} = E^2, \tag{3.2}$$

where the effective potential is given by

$$V_{\mathrm{eff}} = f(\rho)\left(\frac{L^2}{\rho^2} + \xi\right). \tag{3.3}$$

It is also useful to use an analogous mechanical equation for the geometry of the trajectories $r(\phi)$,

$$\left(\frac{d\rho}{d\phi}\right)^2 + W_{\mathrm{eff}}(\rho) = 0, \tag{3.4}$$

where the new effective potential is

$$W_{\mathrm{eff}} = \rho^2 f(\rho) + \frac{\rho^4}{L^2}(\xi f(\rho) - E^2). \tag{3.5}$$

Notice the structural difference of this mechanical equation with respect to the previous one: the particle energy is an additional parameter in the effective potential, while the effective energy always vanishes.

Now let us investigate massive and massless cases.

A. Massive neutral particles ($\xi = 1$)

First, we discuss the simplest types of orbits around the black hole, namely, timelike circular orbits. For these, the radial velocity must vanish, $\dot{\rho}(t) = 0$ for all t, which corresponds to $V_{\mathrm{eff}} = E^2$ and $V'_{\mathrm{eff}}(\rho) = 0$. Stable circular orbits exist if $V''_{\mathrm{eff}}(\rho) > 0$ and the limiting case of this family of orbits is the *innermost stable circular orbit* (ISCO), which is determined by the additional condition of marginal stability, $V''_{\mathrm{eff}}(\rho) = 0$. From $V'_{\mathrm{eff}}(\rho) = 0$ we obtain the following explicit condition for circular orbits:

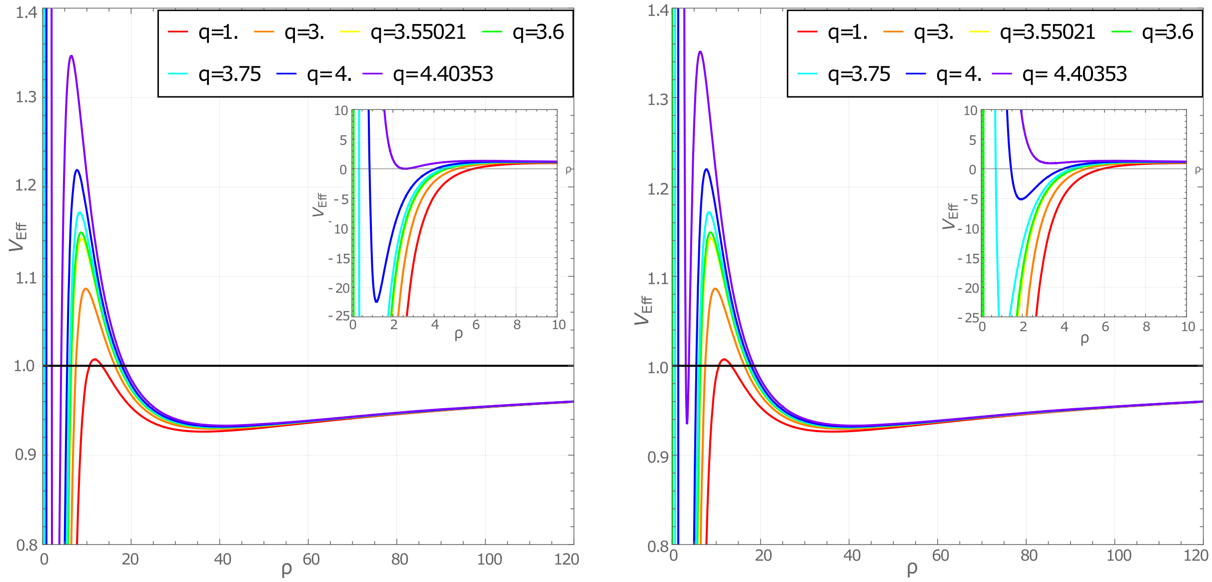

(a) $n = 2$ (b) $n = 3$

FIG. 3. Effective potential for massive particles ($\xi = 1$) vs radius ρ for Y^n BHs with various values of q for n values of 2 and 3 with $m_{\mathrm{BH}} = 3$ and $L = 4m_{\mathrm{BH}}$. Notice that the largest zero of $V_{\mathrm{eff}}(\rho)$ is at the event horizon, and that the minimum of $V_{\mathrm{eff}}(\rho)$, which is relevant to the circular orbits and ISCO, is the shallow one further to the right around $\rho = 40$ in these plots.

$$V'_{\mathrm{eff}}(\rho) = \frac{L^2(1 - 3f(\rho) - \rho^2 K(\rho))}{\rho^3} + \frac{\xi(1 - f(\rho) - \rho^2 K(\rho))}{\rho} = 0, \tag{3.6}$$

where we have used the field Eq. (2.10) for eliminating $f'(\rho)$ from the equation.

For the stability condition we need also the second derivative

$$V''_{\mathrm{eff}}(\rho) = \frac{L^2(12f(\rho) - \rho^3 K'(\rho) + 4\rho^2 K(\rho) - 6)}{\rho^4} - \frac{\xi(2(1 - f(\rho)) + \rho^3 K'(\rho))}{\rho^2}, \tag{3.7}$$

which as mentioned above should be positive. The ISCO is the limiting case of marginal stability, which occurs for $V''_{\mathrm{eff}}(\rho) = 0$ in addition to (3.6). Solving Eq. (3.6) for the angular momentum (which is possible only for $\xi \neq 0$) and substituting in (3.7), we obtain a single equation that determines the ISCO radius ρ_i,

$$V''_{\mathrm{eff}}(\rho_i) = 2\xi \frac{f(\rho_i)(3f(\rho_i) + \rho_i^3 K'(\rho_i) + 7\rho_i^2 K(\rho_i) - 5) + 2(1 - \rho_i^2 K(\rho_i))^2}{\rho_i^2(-3f(\rho_i) - \rho_i^2 K(\rho_i) + 1)} = 0. \tag{3.8}$$

An equivalent equation can be obtained by recognizing that the ISCO radius corresponds to the minimum of the angular momentum function obtained by solving Eq. (3.6), as mentioned above. The ISCO radius thus obtained is independent of the orbit parameters (like L and E). It depends only on the BH characteristics, n, q, and m_{BH}.

Since for our Y^n BHs the radial dependence of all quantities is not explicit, but is given in a parametric form using the additional radial relation $\rho(y)$ of (2.11), all the quantities in this equation are actually functions of y, or should be expressed as such, like $K'(\rho) = dK/d\rho$ using the explicit form (2.12) for $K(y)$. After doing that, one solves Eq. (3.8) with respect to y_i, the parametric value corresponding to the ISCO, and then obtains the associated ISCO radius as $\rho_i = \rho(y_i)$.

In Fig. 3 we have plotted the effective potential for massive particles with a given angular momentum for different cases. We observe that depending on the nonlinearity parameter n and charge q one has a different nontrivial orbital structure. For low charge values (up to $q = 3$) we have a Schwarzschild-like behavior, a single infinitely deep potential well near the horizon and a second shallow binding potential relatively far from the horizon. Beyond these lower values, we have an intermediary state where we see the development of a double minima structure with the interior one fully inside the horizon. In this

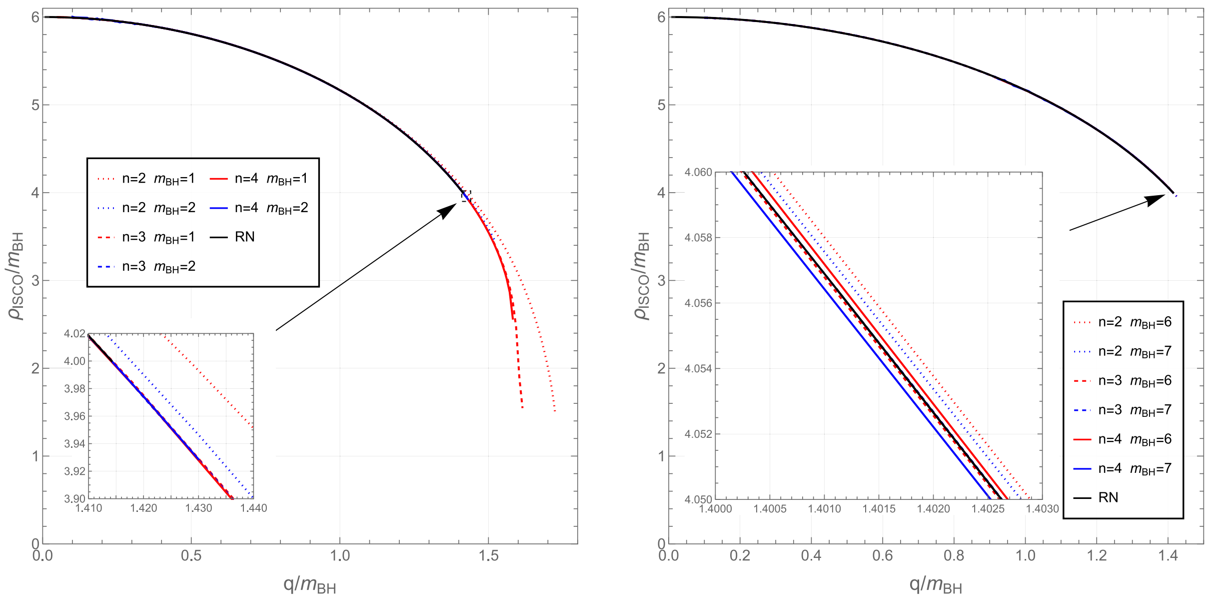

(a) $m_{\rm BH} = 1$ (red) and 2 (blue)

(b) $m_{\rm BH} = 6$ (red) and 7 (blue)

FIG. 4. Mass-scaled radius of the innermost stable circular orbit $\rho_{\rm ISCO}/m_{\rm BH}$ as a function of the scaled charge $q/m_{\rm BH}$ for different black hole masses and index n. The curves indicate that the model approaches scale invariance at larger masses.

configuration there emerges a potential barrier between the inner and outer wells. As the BH charge increases, both potential wells become shallower, as the black hole's grip on orbiting particles weakens due to the repulsive gravitational contribution of the electromagnetic field.

Furthermore, in Fig. 4 we present the behavior of the ISCO radius as a function of the BH mass and charge. We recall the scaling feature of the RN BHs under $(r \to r/M, Q \to Q/M)$, which yields a universal relation between the ISCO radius scaled by the BH mass, $r_{\rm ISCO}/M$, and the similarly scaled charge Q/M,

$$\frac{Q^2}{M^2} = \frac{r_{\rm ISCO}}{M}\left(\frac{9}{4} - \sqrt{\frac{r_{\rm ISCO}}{M} - \frac{15}{16}}\right). \tag{3.9}$$

As can be seen from Eqs. (2.11) and (2.13), this scaling feature does not remain exact in our model, but it is still valid approximately, and is useful for presentation of the results. So, in Fig. 4 we plot the ratio $\rho_{\rm ISCO}/m_{\rm BH}$ as a function of $q/m_{\rm BH}$ for several mass values, which causes a splitting between the various curves. The overall trends can be inferred directly from Fig. 4 and are also supported by the numerical results summarized in Table I for small q and $m_{\rm BH}$. From the table, one observes that increasing $m_{\rm BH}$ at fixed q shifts $\rho_{\rm ISCO}$ inward, consistent with the expectation that a more massive black hole strengthens the gravitational attraction. Similarly, increasing q at fixed $m_{\rm BH}$ shifts the ISCO outward, indicating that in the PINLED framework the electromagnetic contribution effectively weakens the net attraction, pushing $\rho_{\rm ISCO}$ to larger values. We compare the PINLED results with the RN limit. For this purpose, we express the RN lapse function as

$$f_{\rm RN}(y) = 1 - \frac{2m_{\rm BH}}{\rho(y)} + \frac{q^2}{2\rho^2(y)}, \tag{3.10}$$

using the same parametric representation of the radial coordinate $\rho(y)$ defined in Eq. (2.11) and the same rescaling by the natural field parameter $\mathfrak{E}$ and length parameter ℓ defined above Eq. (2.9). For the RN case we employ the same ISCO criterion based on Eq. (3.8) with $f_{\rm RN}(y)$ given above and $K_{\rm RN}(y) = y/4$.

Alternatively, we can use the fact that this adapted form of the RN metric, $f_{\rm RN}(y)$, naturally "inherits" the RN scaling feature mentioned above, with the necessary adaptations to the dimensionless quantities $m_{\rm BH}$, q, and $\rho(y)$. Consequently, $\rho_{\rm ISCO}/m_{\rm BH}$ and $q/m_{\rm BH}$ will satisfy the same relation (3.9) with the obvious replacements. From Fig. 4 we observe that increasing the black hole mass reduces the EBH charge-over-mass, above which naked singularities occur, approaching the RN critical value (which is $\sqrt{2}$ in our units). Accordingly, for $m_{\rm BH} = 1$ and 2 in Fig. 4(a), the curves extend beyond the RN critical charge. In addition, the largest deviation from the RN behavior occurs for $n = 2$, while increasing n shifts the curves closer to the RN limit.

In the next sections we will see that massless particles are more likely to tell Y^n BHs apart from RN ones, since they can "penetrate" closer to the BH horizons, i.e., to the regions where the differences between the metric tensors of both kinds of BHs are more noticeable. Still, the deviations

TABLE I. ISCO values for PINLED Y^n black holes and RN metric for low q and $m_{\rm BH}$ range.

	RN			PINLED ($n=2$)		
q	$m_{\rm BH}=0.2$	$m_{\rm BH}=0.3$	$m_{\rm BH}=0.4$	$m_{\rm BH}=0.2$	$m_{\rm BH}=0.3$	$m_{\rm BH}=0.4$
0.1	1.16163	1.77475	2.38115	1.16229	1.77483	2.38116
0.2	1.03329	1.69570	2.32326	1.04793	1.69729	2.32360
0.3	0.709808	1.54994	2.22182	0.862759	1.56128	2.22392

	PINLED ($n=3$)			PINLED ($n=4$)		
q	$m_{\rm BH}=0.2$	$m_{\rm BH}=0.3$	$m_{\rm BH}=0.4$	$m_{\rm BH}=0.2$	$m_{\rm BH}=0.3$	$m_{\rm BH}=0.4$
0.1	1.16164	1.77475	2.38115	1.16163	1.77475	2.38115
0.2	1.03463	1.69572	2.32326	1.03339	1.69570	2.32326
0.3	0.804013	1.55035	2.22184	0.775924	1.54995	2.22182

of the Y^n BHs with respect to the RN ones will diminish with increasing charge and mass.

B. Massless particles $\xi = 0$

In this subsection, we focus on the motion of massless (neutral) particles moving along null geodesics, such as photons. This is done by setting $\xi = 0$ in Eqs. (3.3) and (3.5), which simplifies the effective potential to

$$V_{\rm eff} = f(\rho)\left(\frac{L^2}{\rho^2}\right), \tag{3.11}$$

as well as the associated effective potential for light rays [i.e., $r(\phi)$] to

$$W_{\rm eff} = \rho^2 f(\rho) - \rho^4/b^2, \tag{3.12}$$

where $b = L/E$ is the impact parameter of a light ray. In what follows we will use both kinds of effective potential according to our convenience.

The effective potential $V_{\rm eff}(\rho)$ can exhibit both minima and maxima corresponding to stable and unstable circular orbits, respectively. The potential for massless particles typically admits both, but outside the horizon there is only a single maximum that corresponds to unstable circular orbits. These orbits comprise the photon sphere (or photon ring in $2+1$ dimensions), where the centrifugal repulsion is exactly balanced by the gravitational attraction.

In Fig. 5 we can see the profile of effective potential $V_{\rm eff}(\rho)$ of Y^n black holes for various values of n with a given angular momentum. The minima that correspond to stable photon orbits are hidden behind the horizon, which is located at the exterior root of $V_{\rm eff}(\rho)$. Furthermore, as expected, we observe an evolution from a Schwarzschild-like profile

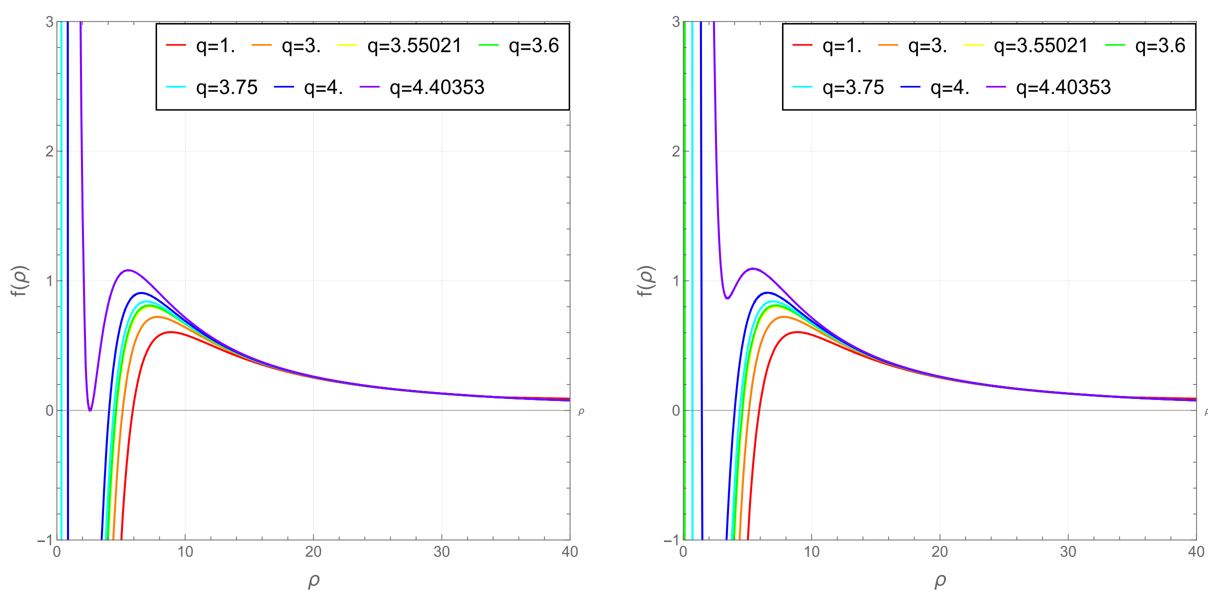

(a) $n=2$ (b) $n=3$

FIG. 5. Effective potential $V_{\rm eff}(\rho)$ for massless particles ($\xi = 0$) for Y^n BHs with various values of q for n values of 2 and 3 with $m_{\rm BH} = 3$. The photon spheres correspond to the static unstable $\rho(\lambda)$ "sitting" at the top of the potential hill.

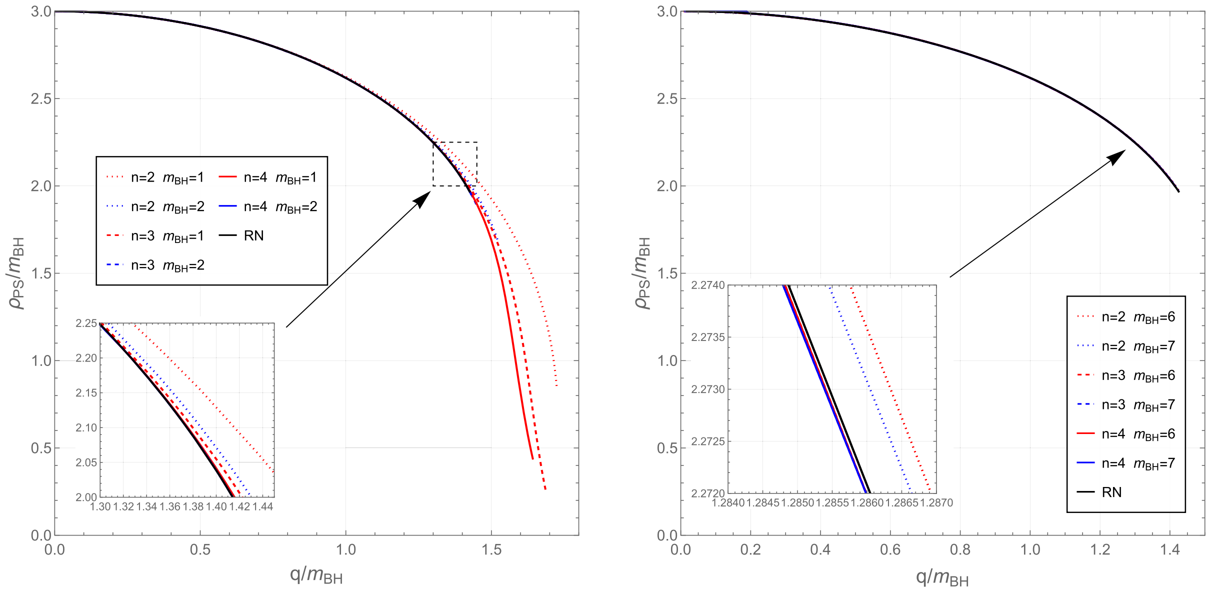

(a) $m_{\rm BH} = 1$ (red) and 2 (blue) (b) $m_{\rm BH} = 6$ (red) and 7 (blue)

FIG. 6. Mass-scaled radius of the photon sphere $\rho_{\rm PS}/m_{\rm BH}$ as a function of the scaled charge $q/m_{\rm BH}$ for different black hole masses and index n.

(low q) to a more oscillatory profile with an additional turning point as q increases.

The condition for circular null geodesics is obtained by requiring that the radial acceleration vanishes, which is equivalent to extremizing the effective potential $dV_{\rm eff}/d\rho = 0$, as we saw already for massive particles. For the potential (3.11) for null geodesics this yields

$$V'_{\rm eff} = \frac{L^2}{\rho^3}(\rho f'(\rho) - 2f(\rho)) = 0. \Rightarrow \rho_{ps} f'(\rho_{ps}) = 2f(\rho_{ps}). \tag{3.13}$$

Furthermore, using the field Eq. (2.10) we may eliminate $f'(\rho)$ and obtain a simple algebraic relation for the photon sphere radius ρ_{ps}, which can also be obtained directly from the rhs of (3.6) with $\xi = 0$,

$$1 - 3f(\rho_{ps}) - \rho_{ps}^2 K(\rho_{ps}) = 0. \tag{3.14}$$

More useful for our Y^n solutions, which utilize parametric representation, is (3.14) rewritten in terms of y, or its alternative version written in terms of y and the mass function,

$$\frac{6m(y_{ps})}{\rho(y_{ps})} - \rho^2(y_{ps})K(y_{ps}) - 2 = 0. \tag{3.15}$$

For given solutions y_{ps} of Eq. (3.15) one can obtain the corresponding photon sphere radius ρ_{ps} with the condition $\rho_{ps} > \rho_H$. We note that like the ISCO radius, the photon sphere radius is independent of the specific orbital parameters, but depends only on the BH characteristics, n, q, and $m_{\rm BH}$. As before, we will perform scaling by the BH mass and present $\rho_{\rm ps}/m_{\rm BH}$ as a function of $q/m_{\rm BH}$ for various $m_{\rm BH}$ values.

In Fig. 6, we present the variation of the scaled photon sphere radius $\rho_{\rm ps}/m_{\rm BH}$ as a function of the scaled charge $q/m_{\rm BH}$ for several fixed black hole masses and values of the nonlinearity index n. For a given mass, $\rho_{\rm ps}$ decreases monotonically as the charge increases. We observe that $\rho_{\rm ps}$ in the Y^n and RN spacetimes exhibits qualitatively similar behavior over most of the parameter space. For lower mass values, the EBH charge above which naked singularities occur is larger than in the RN case. Consequently, the Y^n photon sphere continues to decrease monotonically up to this critical charge, remaining asymptotically above the horizon, as illustrated for $m_{\rm BH} = 1$ in Fig. 6(a). For larger values of both the nonlinearity index n and the mass $m_{\rm BH}$, the profile becomes indistinguishable from that of the RN black hole.

C. Shadow radius

In the era of very-long-baseline interferometry, which gave us the first images of the supermassive black holes M87* and SgrA*, the concept of the black hole "shadow" has become a central observable in testing strong-field gravity. The shadow is not the event horizon itself, but a dark silhouette cast against the bright, lensed background emission of the surrounding accretion flow. This silhouette appears because photons with sufficiently small impact parameters fall into the black hole, creating a region of

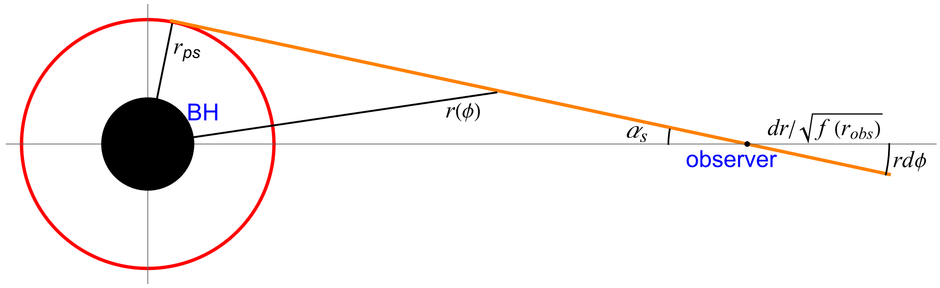

FIG. 7. Illustration of shadow calculation from the observer's position r_{obs}. The shadow angle α_s is the angle between the limiting light ray [which arrives from the photon sphere (radius r_{ps}) at the observer] and the radial direction. The infinitesimal angular and radial lengths are calculated at $r = r_{\text{obs}}$.

photon capture. The boundary of this dark region is defined by the critical photon orbits.

For a distant observer, the shadow is a circular (or nearly circular) disk whose apparent radius is governed by the innermost photon orbits. A key quantity for describing these orbits is the impact parameter $b = L/E$ defined already in the previous subsection. As we have shown there, unstable photon circular orbits exist at a critical radius ρ_{ps}. The corresponding critical impact parameter b_{crit} separates photons that fall into the black hole from those that escape to infinity. In asymptotically flat spacetimes, this critical impact parameter directly corresponds to the shadow radius r_s observed at infinity. For our spherically symmetric line element (2.9), we can easily relate the shadow radius to the photon sphere quantities. For that we notice that the critical light rays that arrive at the observer are those that connect the photon sphere and the observer represented by the ray shown in Fig. 7. The angle α between such a light ray and the radial direction at the location of the observer satisfies the following relation written in terms of the dimensionless radial variable:

$$\cot^2\alpha = \left(\frac{d\rho/\sqrt{f(\rho_{\text{obs}})}}{\rho_{\text{obs}}d\phi}\right)^2 = \frac{1}{\rho_{\text{obs}}^2 f(\rho_{\text{obs}})}\left(\frac{d\rho}{d\phi}\right)^2\Bigg|_{\rho=\rho_{\text{obs}}}$$
$$= \frac{-W_{\text{eff}}(\rho_{\text{obs}})}{\rho_{\text{obs}}^2 f(\rho_{\text{obs}})}, \tag{3.16}$$

where for the last term we used Eq. (3.4). Actually, this expression is still valid for any light ray that arrives at the observer. In order to specify in light rays that connect the observer with the photon sphere, we need to pick up the impact parameter b_{crit}, which yields $W_{\text{eff}}(\rho_{ps}) = 0$, and use that value in $W_{\text{eff}}(\rho_{\text{obs}})$. Looking at the relevant expression (3.12), we find immediately that $b_{\text{crit}}^2 = \rho_{ps}^2/f(\rho_{ps})$, and by substituting in (3.16) we obtain

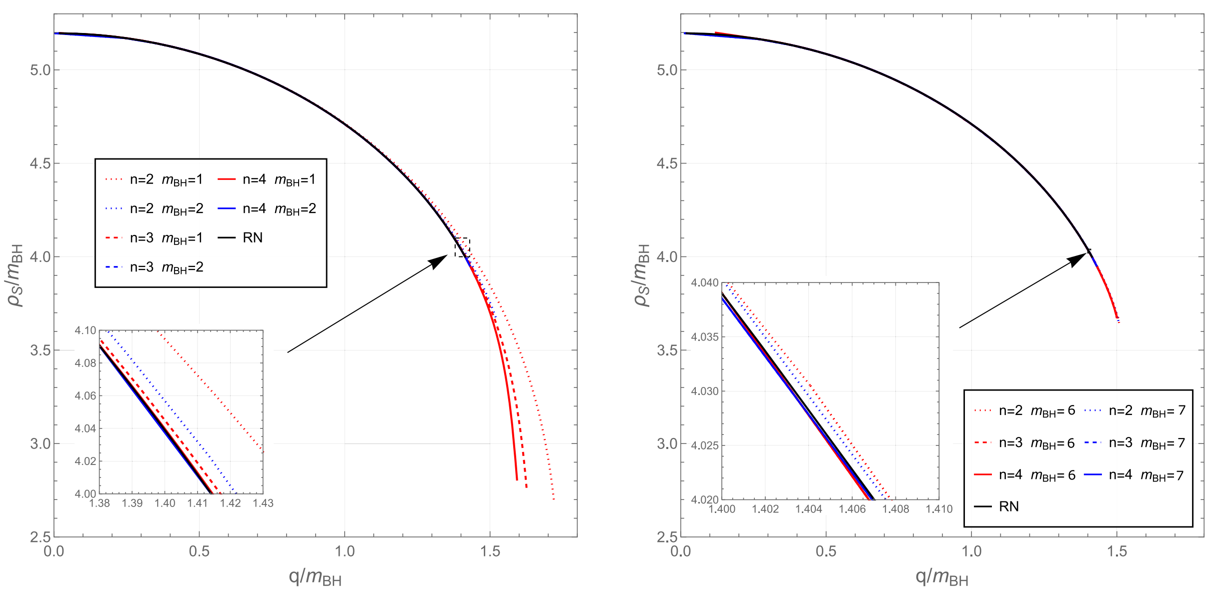

(a) $m_{\text{BH}} = 1$ (red) and 2 (blue)

(b) $m_{\text{BH}} = 6$ (red) and 7 (blue)

FIG. 8. Mass-scaled shadow radius ρ_S/m_{BH} as a function of the scaled charge q/m_{BH} for different black hole masses and index n.

$$\sin^2\alpha_s = \frac{\rho_{ps}^2}{f(\rho_{ps})}\frac{f(\rho_{\rm obs})}{\rho_{\rm obs}^2}. \tag{3.17}$$

The radius of the BH shadow for an observer at a large distance can be obtained using Eq. (3.17) as

$$\rho_s \simeq \rho_{\rm obs}\sin\alpha_s \simeq \frac{\rho_{ps}}{\sqrt{f(\rho_{ps})}}\sqrt{f(\rho_{\rm obs})}, \tag{3.18}$$

so the shadow radius as perceived by a static observer at infinity is given by

$$\rho_s = \frac{\rho_{ps}}{\sqrt{f(\rho_{ps})}}. \tag{3.19}$$

In the context of the PINLED model, using (3.14) we obtain the expression for the shadow radius as

$$\rho_s = \frac{\sqrt{3}\rho(y_{ps})}{\sqrt{1-\rho^2(y_{ps})K(y_{ps})}} \tag{3.20}$$

for use in parametric representation.

From Fig. 8, we observe that the scaled shadow radius decreases monotonically with increasing charge-over-mass. In the low-mass, low-n regime, there is a clear deviation from the RN curve. However, for larger black hole masses, the model approaches the RN behavior, and the profiles become indistinguishable.

IV. LIGHT DEFLECTION ANGLES

In this section we will turn to unbound trajectories and analyze light deflection resulting from PINLED Y^n BHs. The trajectories of a photon moving in a static, spherically symmetric spacetime can be conveniently analyzed using orbital Eq. (3.4) with the effective potential (3.12),

$$\left(\frac{d\rho}{d\phi}\right)^2 + \rho^2 f(\rho) - \frac{\rho^4}{b^2} = 0, \tag{4.1}$$

where $b = L/E$. The turning point of the trajectory corresponds to the point of closest approach ρ_m, where the radial component of the photon's four-velocity vanishes. Thus, by applying Eq. (4.1) to $\rho = \rho_m$ we obtain the following relation among ρ_m and b:

$$\left(\frac{d\rho}{d\phi}\right)^2\bigg|_{\rho=\rho_m} = 0 \Rightarrow \frac{1}{b^2} = \frac{f(\rho_m)}{\rho_m^2}. \tag{4.2}$$

Therefore, we can use this relation to calculate first the asymptotic direction of a light ray with respect to the direction of its closest approach, which we are free to choose as $\phi = 0$,

$$\Delta\phi = \int_{\rho_m}^{\infty}\frac{d\rho}{\sqrt{\frac{\rho^4}{\rho_m^2}f(\rho_m) - \rho^2 f(\rho)}}. \tag{4.3}$$

For a trajectory symmetric about the point of closest approach, the deflection angle δ of a light ray with respect

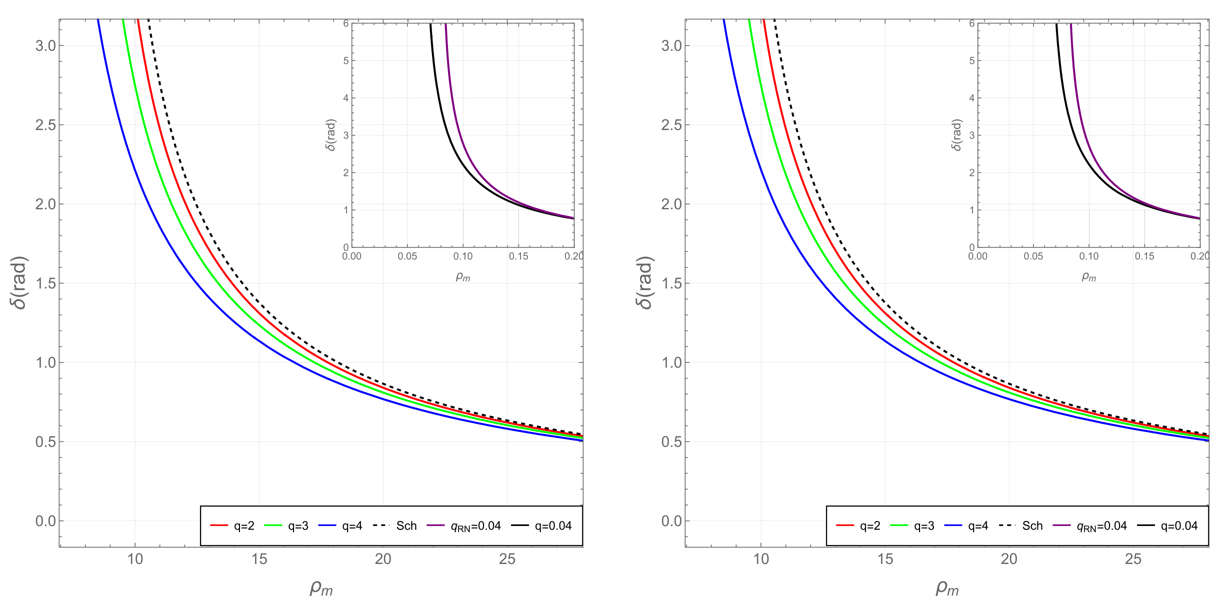

(a) $n = 2$ (b) $n = 3$

FIG. 9. Light deflection angle δ (in radians) vs closest approach ρ_m for $m_{\rm BH} = 3$ and various q values. Dashed black lines represent the Schwarzschild ($q = 0$) case. The inserts present a comparison between RN (black) and Y^n (purple) cases, both with small charge and mass values where the difference is visible: $q = 0.04$ and $m_{\rm BH} = 0.03$.

to its asymptotic incoming direction can be written as

$$\delta = 2\Delta\phi - \pi. \tag{4.4}$$

As always, the integral for $\Delta\phi$ in (4.4) should be calculated for deflection by Y^n BHs after the change of variables $\rho(y)$. The deflection angle is specific to the light trajectory characterized by ρ_m, or alternatively by the impact parameter b. Figure 9 illustrates the variation of the deflection angle δ (in radians) as a function of the closest approach distance ρ_m for light deflection by the Y^n BHs, considering different nonlinearity orders $n = 2$, 3, and 4. The results are compared with the Schwarzschild and RN cases, shown, respectively, by the dashed and solid black curves, for a fixed black hole mass $m_{\rm BH} = 3$. As expected, the deflection angle increases sharply as ρ_m approaches the photon sphere radius ρ_{ps}, where the light ray winds around the BH with an increasingly large number of times. Since the photon sphere radii depend on the BH parameters, each curve has a different divergence point. For larger and increasing ρ_m, the deflection angle decreases monotonically, and all curves converge to the weak deflection regime where $\delta \to 0$ asymptotically. Increasing the charge q leads to a stronger deviation from the Schwarzschild curve, reducing the deflection angle at a given ρ_m. This reflects the repulsive PINLED contribution to the effective gravitational pull, which effectively weakens the light deflection by Y^n BHs. However, a comparison with the RN case shows that the deflection angle remains essentially unchanged at high charge values, while deviations become appreciable for sufficiently small charges. We also note that the difference between the two curves of the deflection angle increases while approaching from large distances to the photon sphere. This is also consistent with the observation that the departure of the Y^n metric tensor from the RN one also increases toward the center.

V. PERIASTRON PRECESSION

In this section, we present a general and systematic derivation of the periastron precession within the PINLED model. We focus on the motion of massive test particles, corresponding to the substitution $\xi = 1$ in Eqs. (3.3) and (3.5). Equations (3.4) and (3.5) together constitute the first-order "mechanical" equation, which determines the geometrical shape of the orbits $\rho(\phi)$. The equation for massive test particles is

$$\left(\frac{d\rho}{d\phi}\right)^2 = -\rho^2 f(\rho) - \frac{\rho^4}{L^2} f(\rho) + \frac{E^2}{L^2}\rho^4 \equiv -W(\rho), \tag{5.1}$$

where we denote here by $W(\rho)$ the effective potential with $\xi = 1$. For studying the periastron precession we focus on bound (but not necessarily closed) orbits. The two radial turning points of these orbits are determined by the condition $W(\rho) = 0$. These roots define the extrema of the radial motion, with ρ_- corresponding to the periastron and ρ_+ to the apastron.

The angular displacement accumulated as the particle moves from the periastron to the apastron is obtained by integrating $d\phi/d\rho$ using the explicit Eq. (5.1), between the corresponding turning points. The total angular advance over one complete radial oscillation (periastron to apastron and back) is, therefore, given by

$$\Phi = 2\int_{\rho_-}^{\rho_+} \frac{d\rho}{\sqrt{-W(\rho)}}. \tag{5.2}$$

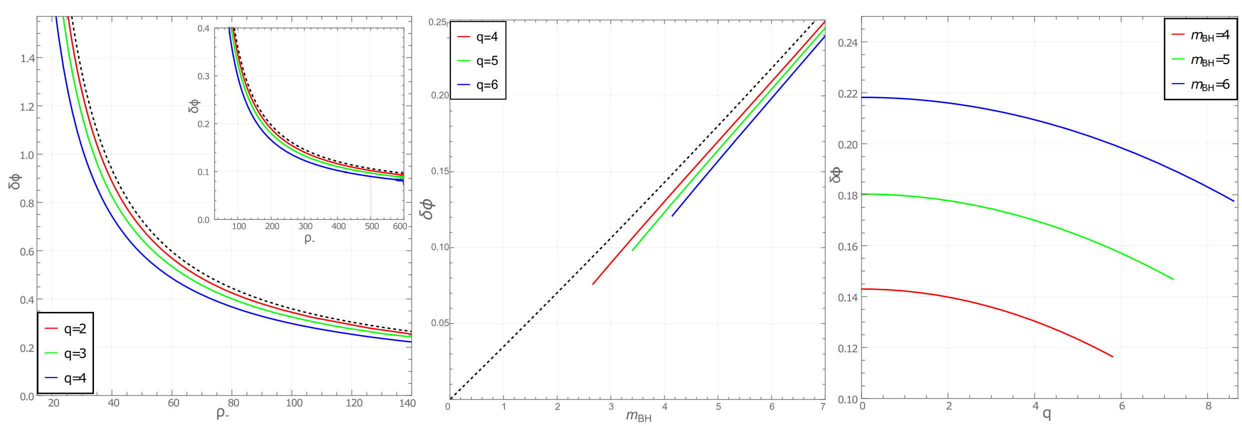

(a) $\delta\phi$ vs ρ_- for $n = 2$ with $\rho_+ = 600$ and $m_{BH} = 3$.

(b) $\delta\phi$ vs m_{BH} for $n = 2$ with $\rho_+ = 600$ and $\rho_- = 500$.

(c) $\delta\phi$ vs q for $n = 2$ with $\rho_+ = 600$ and $\rho_- = 500$.

FIG. 10. Periastron precession $\delta\phi$ as a function of the periastron radius ρ_-, mass $m_{\rm BH}$, and the charge parameter q for Y^n BHs for fixed apastron values. The black dashed curves in (a) and (b) correspond to the Schwarzschild BHs, and the $q = 0$ values of the curves on the vertical axis in (c) represent the Schwarzschild precession values with the corresponding $m_{\rm BH}$.

TABLE II. Periastron precession $\delta\phi$ for various values of n, q, and $m_{\rm BH}$ for $\rho_- = 500$ and $\rho_+ = 600$.

	RN			PINLED ($n=2$)		
q	$m_{\rm BH}=3$	$m_{\rm BH}=4$	$m_{\rm BH}=5$	$m_{\rm BH}=3$	$m_{\rm BH}=4$	$m_{\rm BH}=5$
1	0.10528	0.14218	0.17961	0.10528	0.14217	0.17960
3	0.09707	0.13588	0.17445	0.09705	0.13587	0.17445
4	0.08987	0.13036	0.16994	0.08986	0.13034	0.16994

	PINLED ($n=3$)			PINLED ($n=4$)		
q	$m_{\rm BH}=3$	$m_{\rm BH}=4$	$m_{\rm BH}=5$	$m_{\rm BH}=3$	$m_{\rm BH}=4$	$m_{\rm BH}=5$
1	0.10524	0.14214	0.17957	0.10523	0.14213	0.17956
3	0.09677	0.13588	0.17445	0.09667	0.13545	0.17401
4	0.08938	0.12981	0.16936	0.08922	0.12963	0.16917

For a closed (periodic) Keplerian orbit one would have $\Phi = 2\pi$—any deviation from this value signals the presence of periastron precession. Accordingly, the periastron shift per orbit is defined as

$$\delta\phi = \Phi - 2\pi = 2\int_{\rho_-}^{\rho_+} \frac{d\rho}{\sqrt{-W(\rho)}} - 2\pi. \tag{5.3}$$

Notice that the integration limits ρ_- and ρ_+ are determined by the orbit parameters: energy E and angular momentum L. This is done from the two solutions of the equation $W(\rho_\pm) = 0$ mentioned above. However, it is easier to do the converse and solve the same equations for E and L in terms of ρ_- and ρ_+. The result is

$$E^2 = \frac{f(\rho_-)f(\rho_+)(\rho_-^2 - \rho_+^2)}{f(\rho_+)\rho_-^2 - f(\rho_-)\rho_+^2}, \quad L^2 = \frac{[f(\rho_-) - f(\rho_+)]\rho_-^2\rho_+^2}{f(\rho_+)\rho_-^2 - f(\rho_-)\rho_+^2}. \tag{5.4}$$

For a given orbital configuration specified by the turning points ρ_- and ρ_+, these expressions allow the conserved quantities to be determined uniquely. Substituting Eq. (5.4) into Eq. (5.3), one can compute the periastron precession for any bound orbit in any static, spherically symmetric spacetime characterized by a lapse function $f(\rho)$. In the present context of PINLED Y^n BHs, we have to adapt these results for the parametric representation that we are using. This is done in a straightforward way by the change of variables $\rho(y)$ in the integration in Eq. (5.3) together with changing the integration limits from ρ_- and ρ_+ to their corresponding values y_- and y_+.

Figure 10 displays the periastron precession $\delta\phi$ for Y^n black holes as a function of the periastron radius ρ_-, black hole mass $m_{\rm BH}$, and charge q with fixed apastron ρ_+. In Fig. 10(a), $\delta\phi$ decreases monotonically with respect to ρ_- for fixed $m_{\rm BH}$ and several values of q. Increasing q yields smaller precession for fixed ρ_-. We notice that at the end points of the curves, which correspond to circular orbits, $\delta\phi$ does not vanish. This is a well-known peculiarity of the precession angle. Figure 10(b) shows that $\delta\phi$ grows with $m_{\rm BH}$ similarly to the Schwarzschild case, nearly linear in $m_{\rm BH}$ for fixed q. The three curves for different q values remain closely spaced, demonstrating that the charge contribution is a subdominant correction to the mass term, since for fixed q, the mass can grow indefinitely and the metric becomes closer to Schwarzschild. On the other hand, the charge value has a bound of the order of $m_{\rm BH}$. Figure 10(c) illustrates the dependence on q at fixed $m_{\rm BH}$ and ρ_-, where the precession decreases gradually with increasing q. This is qualitatively in line with the RN result, where the charge introduces a retrograde correction to the precession angle. For the higher n values, $n = 3$ and $n = 4$, the precession results are indistinguishable from the $n = 2$ case within the resolution of the plot. Table II compares the periastron precession between the RN and PINLED models for the same ρ_+ and ρ_- across various values of n, q, and $m_{\rm BH}$. One can see a systematic deviation in PINLED values that grows with both n and q. In all cases, $\delta\phi$ increases with $m_{\rm BH}$ and decreases with q.

VI. CONCLUSION

In this work our main aim was to provide a systematic and self-contained set of strong and weak-field observables for the static, spherically symmetric PINLED Y^n black hole solutions minimally coupled to Einstein-Hilbert gravity. Motivated by the EHT era, where photon ring/shadow measurements and precision lensing tests increasingly probe the near-horizon geometry, we analyzed null and timelike geodesics in the spacetime defined by Eqs. (2.9), (2.11), (2.13), and (2.14), and quantified how the charge parameter q and the nonlinearity index n deform the photon sphere, the shadow size, and the characteristic radii governing massive particle motion, like the ISCO and perihelion precession angle.

For timelike geodesics, we determined circular orbits and the ISCO from $V'_{\rm eff} = 0$ and $V''_{\rm eff} = 0$, obtaining the compact condition (3.8) and solving it for $\rho_{\rm ISCO}$ as a function of mass, charge, and the index n, as shown in Sec. III A. Table III demonstrates that $\rho_{\rm ISCO}$ decreases with

TABLE III. Characteristic radii ρ_H, ρ_{ISCO}, ρ_{ps}, and ρ_s for different values of the charge parameter q and nonlinearity index $n = 2, 3, 4$, computed for a fixed black hole mass $m_{\mathrm{BH}} = 3$.

	$n=2$				$n=3$				$n=4$			
q	ρ_H	ρ_{ISCO}	ρ_{ps}	ρ_s	ρ_H	ρ_{ISCO}	ρ_{ps}	ρ_s	ρ_H	ρ_{ISCO}	ρ_{ps}	ρ_s
1	5.9155	17.7475	8.8875	15.4425	5.91548	17.7475	8.88748	15.4425	5.91548	17.7475	8.88748	15.4425
3	5.12662	15.5007	7.85661	14.1304	5.12137	15.4993	7.85411	14.12880	5.12132	15.4993	7.8541	14.1288
3.55021	4.66136	14.2943	7.27317	13.4144	4.64298	14.2903	7.26519	13.4095	4.64258	14.2903	7.26515	13.4096
3.6	4.60883	14.1652	7.20899	13.3372	4.58796	14.1608	7.20005	13.3318	4.58747	14.1608	7.2	13.3318
3.75	4.4355	13.7219	7.00031	13.0887	4.40414	13.7158	6.98756	13.0811	4.40316	13.7157	6.98747	13.0811
4	4.07624	12.9592	6.58674	12.6095	4.00442	12.9484	6.56181	12.5953	4.0003	12.9484	6.56156	13.0811

increasing q over the parameter range displayed, tracking the contraction of the characteristic strong-field region and providing an additional, independent probe of the geometry. Since the ISCO sets a key scale for accretion dynamics (e.g., the inner edge of thin disks and the onset of strong-field orbital shear), these shifts translate into potentially observable changes in disk spectra and variability when PINLED corrections are appreciable. In short, both in null and timelike geodesics, we see the inherent electromagnetic repulsive effect.

Our results show that, for fixed black hole mass, increasing the charge parameter q shifts the characteristic radii inward: the horizon radius ρ_H, the photon sphere radius ρ_{ps}, the shadow radius ρ_s, and the ISCO radius ρ_{ISCO} all decrease as q grows. This behavior is consistent with the fact that the nonlinear electromagnetic sector reduces the net attractive pull relative to the Schwarzschild case. Conversely, for fixed q, these radii increase with m_{BH}, as expected from the stronger gravitational field of a more massive source.

Another outcome of our analysis is that the null-geodesic observables analyzed in Secs. III B and III C provide the clearest probe of departures from the Reissner-Nordström geometry. In particular, both ρ_{ps} and ρ_s decrease monotonically with q, while the differences between the PINLED and RN cases become most visible in the low-mass, high-charge regime. By contrast, the ISCO remains very close to the RN prediction over most of the parameter space explored here, especially for $n = 3$ and 4, indicating that timelike circular motion is a comparatively weak discriminator of the nonlinear PINLED corrections. The dependence on the nonlinearity index n is generally subleading compared with the dependence on q. Although increasing n produces small quantitative shifts in the characteristic radii, these corrections remain modest, and for several observables the $n = 3$ and $n = 4$ cases become nearly indistinguishable from the RN limit. This indicates that, within the present family of solutions, the charge parameter is the dominant control parameter for the optical and orbital structure, while the effect of the nonlinear index is comparatively mild.

We also analyzed light deflection in Sec. IV and periastron precession in Sec. V. As usual, the light deflection weakens as the light ray closest approach increases. For fixed closest-approach distance, fixed BH mass, and increasing charge, the light deflection angle decreases from the maximum of the Schwarzschild value in the zero-charge limit, while its dependence on n remains weak. The deviation of light deflection angles for Y^n BHs relative to RN is minute in the weak-field, where ρ_m is large. It becomes distinguishable in the opposite limit where ρ_m gets closer to the photon sphere and especially for small BH masses. Likewise, for bound particle orbits with fixed turning points, the periastron advance increases with m_{BH} but decreases with q, again with only small corrections induced by changing n. These particle observables, ISCO and especially the periastron precession, provide useful consistency checks, but they are less sensitive to the PINLED deformation than the quantities associated with the photon region.

From the more practical observational vantage point we note that for BHs that are characterized by mass and charge only, measuring a single characteristic radius or optical observable by itself generally is not sufficient to determine both the mass and the charge uniquely—an independent measurement of a second observable is needed to break the degeneracy. For example, the photon sphere/shadow radius together with the ISCO radius or another observable, such as light deflection angle/periastron precession, can in principle help disentangle (m, q). For the PINLED BHs there is a third parameter to be fixed, namely, the nonlinearity index n. Thus, for this case a third measurement is required in order to "close on" the model and improve parameter estimation.

Figure 11 contains a graphical summary of the general behavior of the characteristic radii analyzed in this study.

Overall, our results furnish a coherent set of strong- and weak-field calculations for this new class of first-order nonlinear electrodynamics black holes. They show that the most promising signatures of the PINLED Y^n geometry are encoded in null-geodesic observables, especially the photon sphere and the shadow, whereas timelike circular motion and weak-field tests mainly provide secondary constraints. Natural extensions of this work include rotating PINLED solutions, quasinormal-mode and ringdown

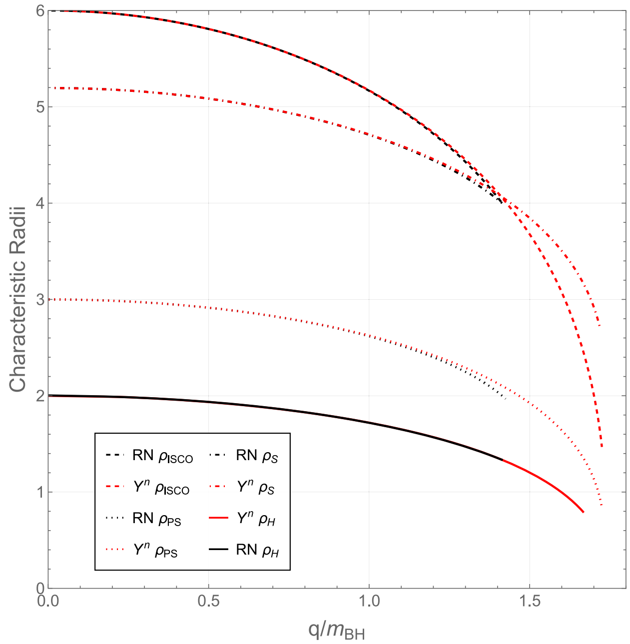

FIG. 11. Characteristic radii (ISCO, photon sphere, shadow, and horizon) as functions of $q/m_{\rm BH}$ for the Y^n model with $n = 2$ and $m_{\rm BH} = 1$ (red), compared to the corresponding RN results (black).

analyses, and the incorporation of realistic emission models and radiative-transfer effects for direct comparison with horizon-scale observations.

ACKNOWLEDGMENTS

İ. İ. Ç. and Y. V. are thankful for the financial support from the Israeli fund for scientific regional cooperation and the Research Authority of the Open University of Israel. A. Ö. would like to acknowledge networking support of the COST Action CA21106—COSMIC WISPers in the Dark Universe: Theory, astrophysics and experiments (CosmicWISPers), the COST Action CA22113—Fundamental challenges in theoretical physics (THEORY-CHALLENGES), the COST Action CA21136—Addressing observational tensions in cosmology with systematics and fundamental physics (CosmoVerse), the COST Action CA23130—Bridging high and low energies in search of quantum gravity (BridgeQG), and the COST Action CA23115—Relativistic Quantum Information (RQI) funded by COST (European Cooperation in Science and Technology). A. Ö. also thanks to EMU, TUBITAK, ULAKBIM (Turkiye), and SCOAP3 (Switzerland) for their support. Y. V. also thanks COST Action CA23130—Bridging high and low energies in search of quantum gravity (BridgeQG).

DATA AVAILABILITY

The data that support the findings of this article are not publicly available. The data are available from the authors upon reasonable request.

[1] R. Abuter *et al.* (GRAVITY Collaboration), Detection of the Schwarzschild precession in the orbit of the star S2 near the Galactic centre massive black hole, Astron. Astrophys. **636**, L5 (2020).

[2] K. Akiyama *et al.* (Event Horizon Telescope Collaboration), First M87 Event Horizon Telescope results. I. The shadow of the supermassive black hole, Astrophys. J. Lett. **875**, L1 (2019).

[3] K. Akiyama *et al.* (Event Horizon Telescope Collaboration), First Sagittarius A* Event Horizon Telescope results. I. The shadow of the supermassive black hole in the center of the Milky Way, Astrophys. J. Lett. **930**, L12 (2022).

[4] T. Johannsen and D. Psaltis, Testing the no-hair theorem with observations in the electromagnetic spectrum: II. Black-hole images, Astrophys. J. **718**, 446 (2010).

[5] A. E. Broderick, T. Johannsen, A. Loeb, and D. Psaltis, Testing the no-hair theorem with Event Horizon Telescope observations of Sagittarius A*, Astrophys. J. **784**, 7 (2014).

[6] T. Johannsen, A. E. Broderick, P. M. Plewa, S. Chatzopoulos, S. S. Doeleman, F. Eisenhauer, V. L. Fish, R. Genzel, O. Gerhard, and M. D. Johnson, Testing general relativity with the shadow size of Sgr A*, Phys. Rev. Lett. **116**, 031101 (2016).

[7] C. Bambi, Testing black hole candidates with electromagnetic radiation, Rev. Mod. Phys. **89**, 025001 (2017).

[8] Z. Younsi, A. Zhidenko, L. Rezzolla, R. Konoplya, and Y. Mizuno, New method for shadow calculations: Application to parametrized axisymmetric black holes, Phys. Rev. D **94**, 084025 (2016).

[9] A. Grenzebach, V. Perlick, and C. Lämmerzahl, Photon regions and shadows of Kerr-Newman-NUT black holes with a cosmological constant, Phys. Rev. D **89**, 124004 (2014).

[10] R. A. Hennigar, M. B. J. Poshteh, and R. B. Mann, Shadows, signals, and stability in Einsteinian cubic gravity, Phys. Rev. D **97**, 064041 (2018).

[11] X.-M. Kuang, Z.-Y. Tang, B. Wang, and A. Wang, Constraining a modified gravity theory in strong gravitational lensing and black hole shadow observations, Phys. Rev. D **106**, 064012 (2022).

[12] T. Bronzwaer and H. Falcke, The nature of black hole shadows, Astrophys. J. **920**, 155 (2021).

[13] S. Vagnozzi, C. Bambi, and L. Visinelli, Concerns regarding the use of black hole shadows as standard rulers, Classical Quantum Gravity **37**, 087001 (2020).

[14] Y. Chen, R. Roy, S. Vagnozzi, and L. Visinelli, Superradiant evolution of the shadow and photon ring of Sgr A*, Phys. Rev. D **106**, 043021 (2022).
[15] R. C. Pantig and A. Övgün, Gravitational black hole shadow spectroscopy, Phys. Rev. D **112**, 124072 (2025).
[16] H. C. D. Lima, Junior., L. C. B. Crispino, P. V. P. Cunha, and C. A. R. Herdeiro, Can different black holes cast the same shadow?, Phys. Rev. D **103**, 084040 (2021).
[17] S. Boyeneni, J. Wu, and E. R. Most, Unveiling the electrodynamic nature of spacetime collisions, Phys. Rev. Lett. **135**, 101401 (2025).
[18] J. L. Synge, The escape of photons from gravitationally intense stars, Mon. Not. R. Astron. Soc. **131**, 463 (1966).
[19] V. Perlick and O. Y. Tsupko, Calculating black hole shadows: Review of analytical studies, Phys. Rep. **947**, 1 (2022).
[20] P. V. P. Cunha and C. A. R. Herdeiro, Shadows and strong gravitational lensing: A brief review, Gen. Relativ. Gravit. **50**, 42 (2018).
[21] V. Bozza, Gravitational lensing in the strong field limit, Phys. Rev. D **66**, 103001 (2002).
[22] K. S. Virbhadra and G. F. R. Ellis, Schwarzschild black hole lensing, Phys. Rev. D **62**, 084003 (2000).
[23] C.-M. Claudel, K. S. Virbhadra, and G. F. R. Ellis, The geometry of photon surfaces, J. Math. Phys. (N.Y.) **42**, 818 (2001).
[24] K. S. Virbhadra, Relativistic images of Schwarzschild black hole lensing, Phys. Rev. D **79**, 083004 (2009).
[25] S. Capozziello, E. Battista, and S. De Bianchi, Null geodesics, causal structure, and matter accretion in Lorentzian-Euclidean black holes, Phys. Rev. D **112**, 044009 (2025).
[26] S. E. Gralla, D. E. Holz, and R. M. Wald, Black hole shadows, photon rings, and lensing rings, Phys. Rev. D **100**, 024018 (2019).
[27] G. Lambiase, D. J. Gogoi, R. C. Pantig, and A. Övgün, Shadow and quasinormal modes of the rotating Einstein–Euler–Heisenberg black holes, Phys. Dark Universe **48**, 101886 (2025).
[28] A. Uniyal, S. Chakrabarti, R. C. Pantig, and A. Övgün, Nonlinearly charged black holes: Shadow and thin-accretion disk, New Astron. **111**, 102249 (2024).
[29] M. Born and L. Infeld, Foundations of the new field theory, Proc. R. Soc. A **144**, 425 (1934).
[30] H. Euler and B. Kockel, The scattering of light by light in Dirac's theory, Naturwiss **23**, 246 (1933).
[31] W. Heisenberg and H. Euler, Consequences of Dirac's theory of positrons, Z. Phys. **98**, 714 (1936).
[32] D. P. Sorokin, Introductory Notes on non-linear electrodynamics and its applications, Fortschr. Phys. **70**, 2200092 (2022).
[33] M. Novello, S. E. Perez Bergliaffa, and J. M. Salim, Singularities in general relativity coupled to nonlinear electrodynamics, Classical Quantum Gravity **17**, 3821 (2000).
[34] G. W. Gibbons and C. A. R. Herdeiro, Born-Infeld theory and stringy causality, Phys. Rev. D **63**, 064006 (2001).
[35] H. A. Gonzalez, M. Hassaine, and C. Martinez, Thermodynamics of charged black holes with a nonlinear electrodynamics source, Phys. Rev. D **80**, 104008 (2009).
[36] B. Toshmatov, Z. Stuchlík, J. Schee, and B. Ahmedov, Electromagnetic perturbations of black holes in general relativity coupled to nonlinear electrodynamics, Phys. Rev. D **97**, 084058 (2018).
[37] J. Bardeen, Non-singular general relativistic gravitational collapse, *Proceedings of the 5th International Conference on Gravitation and the Theory of Relativity* (Pub. House of Tbilisi University, Tbilisi, Georgia, 1968), p. 87.
[38] S. Hayward, Formation and evaporation of regular black holes, Phys. Rev. Lett. **96**, 031103 (2006).
[39] E. Ayon-Beato and A. Garcia, Regular black hole in general relativity coupled to nonlinear electrodynamics, Phys. Rev. Lett. **80**, 5056 (1998).
[40] E. Ayon-Beato and A. Garcia, The Bardeen model as a nonlinear magnetic monopole, Phys. Lett. B **493**, 149 (2000).
[41] E. Ayon-Beato and A. Garcia, New regular black hole solution from nonlinear electrodynamics, Phys. Lett. B **464**, 25 (1999).
[42] K. A. Bronnikov, Regular magnetic black holes and monopoles from nonlinear electrodynamics, Phys. Rev. D **63**, 044005 (2001).
[43] I. Dymnikova, Regular electrically charged structures in nonlinear electrodynamics coupled to general relativity, Classical Quantum Gravity **21**, 4417 (2004).
[44] L. Balart and E. C. Vagenas, Regular black holes with a nonlinear electrodynamics source, Phys. Rev. D **90**, 124045 (2014).
[45] Z.-Y. Fan and X. Wang, Construction of regular black holes in general relativity, Phys. Rev. D **94**, 124027 (2016).
[46] K. A. Bronnikov, Comment on, "Construction of regular black holes in general relativity", Phys. Rev. D **96**, 128501 (2017).
[47] B. Toshmatov, Z. Stuchlík, and B. Ahmedov, Comment on "Construction of regular black holes in general relativity", Phys. Rev. D **98**, 028501 (2018).
[48] M. Hassaine and C. Martinez, Higher-dimensional charged black holes solutions with a nonlinear electrodynamics source, Classical Quantum Gravity **25**, 195023 (2008).
[49] H. Maeda, M. Hassaine, and C. Martinez, Lovelock black holes with a nonlinear Maxwell field, Phys. Rev. D **79**, 044012 (2009).
[50] M. Cataldo and A. Garcia, Three dimensional black hole coupled to the Born-Infeld electrodynamics, Phys. Lett. B **456**, 28 (1999).
[51] M. Cataldo and A. Garcia, Regular $(2+1)$-dimensional black holes within nonlinear electrodynamics, Phys. Rev. D **61**, 084003 (2000).
[52] G. W. Gibbons and D. A. Rasheed, Electric—magnetic duality rotations in nonlinear electrodynamics, Nucl. Phys. **B454**, 185 (1995).
[53] G. W. Gibbons and D. A. Rasheed, Sl(2,R) invariance of nonlinear electrodynamics coupled to an axion and a dilaton, Phys. Lett. B **365**, 46 (1996).
[54] M. Novello, V. A. De Lorenci, J. M. Salim, and R. Klippert, Geometrical aspects of light propagation in nonlinear electrodynamics, Phys. Rev. D **61**, 045001 (2000).
[55] V. A. De Lorenci, R. Klippert, M. Novello, and J. M. Salim, Light propagation in nonlinear electrodynamics, Phys. Lett. B **482**, 134 (2000).
[56] E. F. Eiroa, Gravitational lensing by Einstein-Born-Infeld black holes, Phys. Rev. D **73**, 043002 (2006).

[57] V. Perlick, O. Y. Tsupko, and G. S. Bisnovatyi-Kogan, Influence of a plasma on the shadow of a spherically symmetric black hole, Phys. Rev. D **92**, 104031 (2015).

[58] S. G. Ghosh, A nonsingular rotating black hole, Eur. Phys. J. C **75**, 532 (2015).

[59] B. Toshmatov, Z. Stuchlík, and B. Ahmedov, Generic rotating regular black holes in general relativity coupled to nonlinear electrodynamics, Phys. Rev. D **95**, 084037 (2017).

[60] I. Dymnikova and E. Galaktionov, Regular rotating electrically charged black holes and solitons in non-linear electrodynamics minimally coupled to gravity, Classical Quantum Gravity **32**, 165015 (2015).

[61] R. Kumar, A. Kumar, and S. G. Ghosh, Testing rotating regular metrics as candidates for astrophysical black holes, Astrophys. J. **896**, 89 (2020).

[62] B. Toshmatov, B. Ahmedov, and D. Malafarina, Can a light ray distinguish charge of a black hole in nonlinear electrodynamics?, Phys. Rev. D **103**, 024026 (2021).

[63] K. Akiyama *et al.* (Event Horizon Telescope Collaboration), First M87 Event Horizon Telescope results. VI. The shadow and mass of the central black hole, Astrophys. J. Lett. **875**, L6 (2019).

[64] P. Kocherlakota *et al.* (Event Horizon Telescope Collaboration), Constraints on black-hole charges with the 2017 EHT observations of M87*, Phys. Rev. D **103**, 104047 (2021).

[65] S. Vagnozzi *et al.*, Horizon-scale tests of gravity theories and fundamental physics from the Event Horizon Telescope image of Sagittarius A, Classical Quantum Gravity **40**, 165007 (2023).

[66] A. Allahyari, M. Khodadi, S. Vagnozzi, and D. F. Mota, Magnetically charged black holes from non-linear electrodynamics and the Event Horizon Telescope, J. Cosmol. Astropart. Phys. 02 (2020) 003.

[67] M. Okyay and A. Övgün, Nonlinear electrodynamics effects on the black hole shadow, deflection angle, quasinormal modes and greybody factors, J. Cosmol. Astropart. Phys. 01 (2022) 009.

[68] A. Uniyal, R. C. Pantig, and A. Övgün, Probing a non-linear electrodynamics black hole with thin accretion disk, shadow, and deflection angle with M87* and Sgr A* from EHT, Phys. Dark Universe **40**, 101178 (2023).

[69] G. J. Olmo and D. Rubiera-Garcia, Palatini $f(R)$ black holes in nonlinear electrodynamics, Phys. Rev. D **84**, 124059 (2011).

[70] M. E. Rodrigues, E. L. B. Junior, G. T. Marques, and V. T. Zanchin, Regular black holes in $f(R)$ gravity coupled to nonlinear electrodynamics, Phys. Rev. D **94**, 024062 (2016); Phys. Rev. D **94**, 049904(A) (2016).

[71] M. E. Rodrigues and M. V. de Sousa Silva, Bardeen regular black hole with an electric source, J. Cosmol. Astropart. Phys. 06 (2018) 025.

[72] W. Berej, J. Matyjasek, D. Tryniecki, and M. Woronowicz, Regular black holes in quadratic gravity, Gen. Relativ. Gravit. **38**, 885 (2006).

[73] S. Capozziello, S. De Bianchi, and E. Battista, Avoiding singularities in Lorentzian-Euclidean black holes: The role of atemporality, Phys. Rev. D **109**, 104060 (2024).

[74] S. Rasanen and Y. Verbin, Palatini formulation for gauge theory: Implications for slow-roll inflation, Open J. Astrophys. **6** (2023).

[75] Y. Verbin, B. Pulice, A. Övgün, and H. Huang, New black hole solutions of second and first order formulations of nonlinear electrodynamics, Phys. Rev. D **111**, 084061 (2025).

[76] J. Plebanski, Lectures on Non-Linear Electrodynamics (Nordita, Copenhagen, 1970).